

Numerical Study of Traveling Wave Solutions to 2D Boussinesq Equation

K. Angelow*, N. Kolkovska

*Institute of Mathematics and Informatics, Bulgarian Academy of Sciences, Acad.
G. Bonchev Bl.8, 1113 Sofia, Bulgaria*

Abstract

The aim of this paper is to evaluate stationary propagating wave solutions to the two dimensional Boussinesq equation. To solve the resulting nonlinear fourth order elliptic problem we use a combination of high order finite difference schemes, an iterative procedure and new asymptotic boundary conditions. A number of numerical results are obtained for the validation of the method and for dependence of the wave's shape on the velocity c and dispersion parameters. We give also a comparison with the numerical results and best-fit formulae given in [7, 8].

Keywords: two dimensional Boussinesq equation, traveling wave solutions (TWS), high order finite difference schemes, asymptotic boundary conditions

1. Introduction

In this paper we consider the two dimensional Boussinesq Equation (BE)

$$u_{tt} - \Delta u - \beta_1 \Delta u_{tt} + \beta_2 \Delta^2 u + \Delta f(u) = 0 \quad \text{for } (x, y) \in \mathbb{R}^2, t \in \mathbb{R}^+, \quad (1)$$

$$\begin{aligned} u(x, y, 0) &= u_0(x, y), \quad u_t(x, y, 0) = u_1(x, y) \quad \text{for } (x, y) \in \mathbb{R}^2, \\ u(x, y) &\rightarrow 0, \Delta u(x, y) \rightarrow 0, \quad \text{for } \sqrt{x^2 + y^2} \rightarrow \infty, \end{aligned} \quad (2)$$

where $f(u) = \alpha u^2$, $\alpha > 0$, $\beta_1 > 0$, $\beta_2 > 0$ are dispersion parameters, and Δ is the Laplace operator. The BE is famous with the approximation of shallow water waves or also weakly non-linear long waves. It is often used for simulation of various physical processes e.g. turbulence in fluid mechanics, vibrations in acoustics and, etc. A derivation of the BE from the original Boussinesq system can be found in [6].

The goal of the article is to seek for solutions to (1) of the type $u(x, y, t) = U(x, y - ct)$, which are stationary solitary waves (SSW) traveling in y direction

*Institute of Mathematics and Informatics, Bulgarian Academy of Sciences, Acad.
G. Bonchev Bl.8, 1113 Sofia, Bulgaria
Email address: angelow@mail.bg (K. Angelow)

with velocity c . In a forthcoming paper the SSW will be applied as initial condition (IC) of the hyperbolic BE (1), (2). Thus it is useful to have accurate, flexible and robust IC in order to test various scenarios with two or more traveling waves colliding with each other.

The SSWs to (1) are computed by a Galerkin spectral method in [3, 4]. In [8] a second order finite difference scheme is used, while in [7] the perturbation series method with respect to the small parameter c is applied. Moreover in [7] the resulting numerical solution is approximated by best-fit formulae. These exact expressions are used further as initial conditions in numerical simulations of the unsteady BE (1)-(2), see [2, 9]. It is shown in these papers, that for velocities $c < 0.3$ the resulting SSW disperse in the form of ring wave expanding to infinity or blow up after some period in time. Thus the traveling wave solutions of the hyperbolic equation (1) are very fragile, i.e. the wave easily blow up or fall apart with time. The relationship between the dispersion and nonlinearity in (1) is very sensitive and the balance between them is easily destroyed. Moreover it is well known that in the one dimensional case the solitary waves are unstable for small wave speeds c while they are stable in form for velocities c close to 1.

Having in mind these observations, we focus in this paper on the more accurate evaluation of SSW U to (1), especially for velocities $c > 0.7$, since it is fundamental for the construction of initial data of the unsteady BE (1).

Note that the stationary solitary waves $U(x, y - ct) = u(x, y, t)$ satisfy the following nonlinear fourth order elliptic equation

$$c^2(E - \beta_1 \Delta)U_{yy} = \Delta U - \beta_2 \Delta^2 U - \Delta f(U), \quad (3)$$

where E is the identity operator.

The evaluation of the solution to (3) described here follows the steps presented in [8], but new modifications are introduced to meet the higher requirements reported above.

First, for the numerical solution of (3) we choose to apply an uniform grid with equal step size $h_x = h_y = h$ in the computational domain Ω_h instead of a nonuniform grid. The reason for this is that the computed solutions to (3) will be used as initial conditions in the hyperbolic problem (1) and these solutions will travel in time, thus we have to have more mesh points not only close to the peak of the waves, but everywhere in the computational domain.

In order to increase the precision of the numerical method, we apply finite difference schemes (FDS) with local approximation of forth $O(h^4)$ and sixth $O(h^6)$ order, i.e. we approximate second order spatial derivatives with high order finite differences. These FDS allow one to evaluate the numerical solution with high accuracy on relatively coarse grid.

A new boundary condition on the computational boundary is also used, together with uniform grid and local approximation order of $O(h^4)$ and $O(h^6)$. The numerical solution of the fourth order elliptic problem (3) is replaced with an iterative procedure, which involves solution of an appropriate parabolic type problem at every iteration step. At the end of each iteration procedure the residual (17) of the discrete equation, approximating (4) is of order 10^{-5} , 10^{-6}

and the distance between two consecutive iterations of the solution is of order 10^{-7} , which is much smaller than the discretization step size h .

In the last section we examine the solution shape and the dependence of the solution on the input parameters - the velocity c and the relative dispersion $\beta = \beta_1/\beta_2$. We show that these qualitative properties of the numerical solution are very similar to those given for the numerical solution in [7, 8]. We compare our results with the best-fit (approximating the numerical solution) formulas stated in [7]. The analysis shows that these best-fit formulas do not satisfy the equations in the neighborhood of the origin in the classical sense because their fourth order derivatives have singularities at the origin. The difference (measured in the maximal norm and in L_2 norms) between our numerical solution and the corresponding best-fit formulae is also high, especially for large velocities c .

The paper is organized as follows. In Section 2 we formulate the problem. The numerical method is given in Section 3 and validated in Section 4. Various numerical experiments and a comparison with results in [7, 8] are reported in Section 5.

2. General Formulation

By the change of variables $x = \sqrt{\beta_1}\bar{x}$, $y = \sqrt{\beta_1}\bar{y}$, $U(x, y) = v(\bar{x}, \bar{y})$ equation (3) is rewritten in the form

$$c^2\beta(E - \Delta)v_{\bar{y}\bar{y}} = \beta\Delta v - \Delta^2 v - \beta\Delta f(v) \quad (4)$$

with $\beta = \beta_1/\beta_2$. The solution v to (4) and its derivatives tend to zero as $|x^2 + y^2| \rightarrow \infty$. In the following we use notations x, y instead of \bar{x}, \bar{y} .

If the condition $c^2 < \min(1/\beta, 1)$ holds then (4) is an elliptic equation of fourth order and the linear second order derivatives in (4) form a second order elliptic equation. In this paper we consider velocities c which fulfill this inequality.

Problem (4) can be rewritten as a system of two elliptic equations of second order in different ways. We expect that the derivatives v_{xx} in x direction will be smaller than the derivative v_{yy} in y direction (since the solution travels in y direction). Therefore the equality $v_{yy} = \Delta v - v_{xx}$ is substituted in (4) and, after introducing an auxiliary function w , we obtain the equivalent to (4) system

$$-(1 - c^2\beta)\Delta v + \beta(1 - c^2)v + \alpha\beta v^2 = w, \quad (5)$$

$$-\Delta w = c^2\beta(E - \Delta)v_{xx}. \quad (6)$$

We seek non-trivial solutions to (5)-(6). To avoid the trivial solution we proceed as in [8]: we fix the value of the solution v at the point $(0, 0)$, $v(0, 0) = \theta$ and introduce new functions: $\hat{v} = v/\theta$ and $\hat{w} = w/\theta$. Thus $\hat{v}(0, 0) = 1$ and

$$\begin{aligned} -(1 - c^2\beta)\Delta \hat{v} + \beta(1 - c^2)\hat{v} + \alpha\beta\theta\hat{v}^2 &= \hat{w}, \\ -\Delta \hat{w} &= c^2\beta(E - \Delta)\hat{v}_{xx}. \end{aligned} \quad (7)$$

The value of θ is found from the equation

$$\theta = \frac{(1 - c^2\beta)\Delta\hat{v} - \beta(1 - c^2)\hat{v} + \hat{w}}{\alpha\beta}|_{x=0, y=0}. \quad (8)$$

In order to evaluate numerically the solution to (7) we introduce artificial time, add false time derivatives and get

$$\begin{aligned} \frac{\partial\hat{v}}{\partial t} - (1 - c^2\beta)\Delta\hat{v} + \beta(1 - c^2)\hat{v} + \alpha\beta\theta\hat{v}^2 &= \hat{w}, \\ \frac{\partial\hat{w}}{\partial t} - \Delta\hat{w} &= c^2\beta(E - \Delta)\hat{v}_{xx}. \end{aligned} \quad (9)$$

Thus the solution to the steady coupled elliptic system (7) is replaced by solving the pertinent transient equations (9) until their solutions \hat{v} and \hat{w} cease to change significantly in time.

3. Numerical Method

We turn to the numerical approximation of the system (9) discussed in the previous section. The backbone of the algorithm is described in [8]. The following improvements and modifications have been made in this article: use of uniform grid with more accurate finite difference schemes of fourth and sixth order of approximation and new type of conditions on the external computational boundary [??].

3.1. Finite difference schemes

First we replace the unbounded domain by a sufficiently large computational domain Ω . Due to the obvious symmetry of the problem, we can look for the solution only in the first quadrant $\Omega = [0, L_x] \times [0, L_y]$. Then a uniform grid Ω_h is defined in the following way

$$\Omega_h = \{(x_i, y_j) : x_i = ih, y_j = jh, i = 0, \dots, N_x, j = 0, \dots, N_y\},$$

where the discretization step h satisfies $h = L_x/N_x = L_y/N_y$. In the implementation of the numerical method the step size τ may vary according to the residual of the computed solution. This is a crucial point because it permits to automatize the control of the error. The value of the function v at mesh point x_i, y_j, t_k is denoted by $v_{i,j}^k$.

We discretize the spatial derivatives in (9) using centered finite differences and extending the stencil:

$$v_{\widehat{xx},p}(x) := \frac{1}{h^2} \sum_{i=-p/2}^{p/2} d_i v(x + ih), \quad (10)$$

Here p is equal to 2, 4 or 6. The weights d_i taken from [10] are 1, -2, 1 for $p = 2$, $-\frac{1}{12}, \frac{4}{3}, -\frac{5}{2}, \frac{4}{3}, -\frac{1}{12}$ - for $p = 4$ and $\frac{1}{90}, -\frac{3}{20}, \frac{3}{2}, -\frac{49}{18}, \frac{3}{2}, -\frac{3}{20}, \frac{1}{90}$ - for $p = 6$. The

approximation error of formulae (10) is $O(h^p)$. Replacing the Laplace operator in (9) by the discrete Laplacian

$$\Delta_{h,p}v_{i,j} := (v_{i,j})_{\widehat{xx},p} + (v_{i,j})_{\widehat{yy},p}$$

we obtain finite difference schemes with high order of approximation $O(h^4)$ for $p = 4$ and $O(h^6)$ for $p = 6$. The application of FDS with high order of approximation leads to a high rate of convergence of the method for sufficiently smooth solutions. In this way more accurate solutions can be produced on a coarse grid.

Symmetry conditions are used to impose the values of the discrete Laplacian at mesh points close to $(0, y)$, and $(x, 0)$. Near the computational boundaries $(x, y) : x = L_x$ and $(x, y) : y = L_y$ we do not change the stencil. The discrete Laplacian is defined there by using the values of the discrete solution given in (??), (??) below at points outside the computational domain.

The Euler explicit rule is applied for approximation of time derivatives. The nonlinear terms in (4) are computed on time level t^k . Thus, the numerical solutions at time level t^{k+1} are evaluated directly by the values of the numerical solution at time level t^k :

$$\begin{aligned} \frac{\widehat{v}_{i,j}^{k+1} - \widehat{v}_{i,j}^k}{\tau} - (1 - c^2\beta)\Delta_{h,p}\widehat{v}_{i,j}^k + \beta(1 - c^2)\widehat{v}_{i,j}^k + \alpha\beta\theta(\widehat{v}_{i,j}^k)^2 &= \widehat{w}_{i,j}^k, \\ \frac{\widehat{w}_{i,j}^{k+1} - \widehat{w}_{i,j}^k}{\tau} - \Delta_{h,p}\widehat{w}_{i,j}^k &= c^2\beta(E - \Delta_{h,p})\widehat{v}_{i,j,\widehat{xx},p}^k. \end{aligned} \quad (11)$$

This method for solving equations (7) can be considered also as “the simple iteration method” for solving linear and nonlinear equations (see [11]). Last but not least, in order to start the procedure we need initial values for functions \widehat{v}, \widehat{w} . These initial values are taken from the formulae in [7].

3.2. Time Step Control

It is possible to use varying time step τ to optimize and speed up the algorithm. When the time step becomes too big the solution starts to diverge and becomes jagged. Fortunately these signs appear first in the residual R i.e. it starts to grow and jag simultaneously while the solution is still fine. Arbitrary cross-sections of the residual look like a discrete function which alternates positive with negative values on the grid. This is a clear sign that the time step has to be lowered, otherwise it is increased. Changing the artificial time is done automatically at each iteration by a factor $f_\tau\tau =: \tau_{new}$, where $f_\tau \in (0.72, 1.015)$.

3.3. Stop Criteria

Usually the calculations of \widehat{v}^{k+1} by equations (11) are terminated if

$$\max_{i,j} |\widehat{v}_{i,j}^{k+1} - \widehat{v}_{i,j}^k| < \epsilon \max_{i,j} |\widehat{v}_{i,j}^k|,$$

where ϵ is a prescribed accuracy. But the solution decays with $\sim 1/r^2$ at infinity $r \rightarrow \infty$, $r = \sqrt{x^2 + y^2}$. Thus for large x and y , the following expressions

$$x^2 U(x, 0, t) \sim c_x \quad \text{and} \quad y^2 U(0, y, t) \sim c_y \quad (12)$$

have asymptotics of constant functions c_x and c_y respectively. There exist start points x_s and y_s for which the asymptotic conditions are valid inside the intervals $[x_s, x_{end}]$ and $[y_s, y_{end}]$. Furthermore, (12) are also valid on intervals $[x_m, x_{end}]$ and $[y_m, y_{end}]$, where x_m and y_m are the midpoints i.e. $x_m = (x_s + x_{end})/2$ and $y_m = (y_s + y_{end})/2$.

A polynomial zero order fit is done at each k^{th} successful iteration $k \in N$ for $x_i U(x_i, 0, k\tau)$, $x_i \in [x_m, x_{end}]$ and $y_i U(0, y_i, k\tau)$, $y_i \in [y_m, y_{end}]$. If the fits c_x and c_y

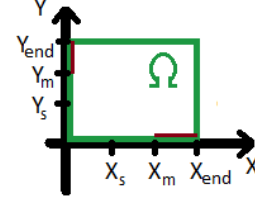


Figure 1: Stop Criteria Intervals

$$|c_x^{k\tau} - c_x^{(k+1)\tau}| < \epsilon \quad \text{and} \quad |c_y^{k\tau} - c_y^{(k+1)\tau}| < \epsilon \quad (13)$$

cease to change significantly in time then the solution has converged.

3.4. Basic Algorithm Steps

The following are the most important mile-stones during the implementation of the algorithm.

- 1) Resolve proper initial condition (v^0, w^0) on the grid Ω_h . Set parameters ϵ and τ .
- 2) Suppose (v^k, w^k) are known.
 - 2.1) Find current θ_k from the discrete approximation of (8);
 - 2.2) Evaluate the solution on the computational boundary;
 - 2.3) Evaluate $\Delta_{h,p} \hat{v}^k$ and $\Delta_{h,p} \hat{w}^k$;
 - 2.4) Calculate $(\hat{v}^{k+1}, \hat{w}^{k+1})$ on the time level t^{k+1} by the Euler explicit scheme (11);
 - 2.5) Calculate the residual $R_{i,j}^{k+1}$ from and check the stop condition (13).
 - 2.6) Control the time step size τ . Set $t^{k+1} = t^k + \tau$.
- 3) Continue steps 2.1) -2.6) with the next time level t^{k+1} till condition (13) is satisfied.

4. Validation

In this section we give several numerical results concerning the verification of the presented numerical method. We use FDS with different approximation errors and several sets of parameters c , α , β , which are shown on each table.

FDS	h	errors E_i in L_2	Conv. Rate	errors E_i in L_∞	Conv. Rate
c=0.45 $O(h^2)$	0.2				
	0.1	0.037705		0.024736	
	0.05	0.008922	2.0794	0.005810	2.0901
c=0.1 $O(h^2)$	0.2				
	0.1	0.015770		0.015794	
	0.05	0.004854	1.6999	0.005243	1.5908
c=0.45 $O(h^4)$	0.2				
	0.1	0.020795		0.008505	
	0.05	0.000278	6.2269	0.000235	5.1800
c=0.1 $O(h^4)$	0.2				
	0.1	0.000892		0.001463	
	0.05	5.4667e-05	4.0281	9.5747e-05	3.9337
c=0.45 $O(h^6)$	0.4				
	0.2	2.0975e-02		2.9341e-02	
	0.1	3.5348e-04	5.8909	5.8346e-04	5.6521
c=0.1 $O(h^6)$	0.4				
	0.2	3.7059e-03		3.7572e-03	
	0.1	7.4723e-05	5.6321	8.3359e-05	5.4942

Table 1: Convergence test for FDS with different approximation errors. Errors E_i are measured in L_2 and L_∞ norms

4.1. Validation of the convergence of the numerical solution

In this series of tests we evaluate the numerical solution of (9) using FDS with approximation errors $O(h^2)$, $O(h^4)$, $O(h^6)$ and parameters $\alpha = 1$, $\beta = 3$, $\epsilon = 10e - 5$, $L_x = 30$, $L_y = 30$. The initial conditions for the artificial parabolic problem (11) are taken from [7]. Using the values of numerical solution on three nested meshes we compute the numerical rate of convergence (Conv. Rate) in L_2 and L_∞ mesh norms by Runge method as $(\log E_1 - \log E_2)/\log 2$. Here $v_{[h]}$, $v_{[h/2]}$ and $v_{[h/4]}$ represent the numerical solution over three nested meshes and $E_1 = \|v_{[h]} - v_{[h/2]}\|$, $E_2 = \|v_{[h/2]} - v_{[h/4]}\|$. Table 1 contains the errors in L_2 and L_∞ norms and the corresponding numerical rate of convergence for the numerical solutions obtained by FDS with second, fourth and sixth order of approximation and velocities $c = 0.1$ or $c = 0.45$. We observe that the experimental rate of convergence approximates well the approximation error of the difference schemes- the FDS are of almost the same order of convergence as the order of approximation. An additional observation is that for the same step size h the schemes with higher order of approximation ($O(h^4)$, $O(h^6)$) lead to a more precise solution than the scheme with $O(h^2)$ approximation error.

4.2. Validation of the new boundary conditions

Two tests are made to verify the new conditions on the computational boundary B . The first one checks important parameters of the numerical procedure from Subsection 3.2. In Table 2 the following quantities are presented at the end of the iteration procedure (11) for several computational domains $L_x = L_y = 20, 40, 80, 160$: the values of the solution v at the point $(0, N_y)$; parameters μ , $\tilde{\mu}$ and the norms $\|v - \bar{v}\|_{2,\hat{\Omega}}$, $\|w - \bar{w}\|_{2,\hat{\Omega}}$, included in the minimization procedure (??). The initial problem is solved with parameters $\alpha = 1$, $\beta = 3$, $c = 0.45$, $\epsilon = 1.0e - 05$, $h = 0.5$.

$L_x = L_y$	v_{0,N_y}	μ	$\tilde{\mu}$	$\ v - \bar{v}\ _{2,\hat{\Omega}}$	$\ w - \bar{w}\ _{2,\hat{\Omega}}$
20	-2.23e-04	1.9355e-01	1.9353e-01	4.17e-05	9.75e-05
40	-5.65e-05	1.9370e-01	1.9369e-01	4.42e-06	1.03e-05
80	-1.41e-05	1.9378e-01	1.9378e-01	7.56e-07	1.79e-06
160	-3.53e-06	1.9381e-01	1.9381e-01	7.44e-10	1.40e-09

Table 2: Characteristic parameters of the minimization procedure (??) for different computational domains

The results in Table 2 demonstrate that parameters μ and $\tilde{\mu}$ converge as the domain becomes larger. The values of v (shown in the second column in Table 2) decay with a rate of $1/r^2$.

The second test reveals the asymptotics of the numerical solution presented in log-log plots. Pictures in Figure 2 demonstrate important aspects of solution's cross sections on four different grids. The size of the computational domain $[0, 50] \times [0, 50]$ is kept constant and only the step h changes, $h = 0.1, 0.2, 0.4, 0.8$. We set the following parameters: $\alpha = 1$, $\beta = 3$, $c = 0.45$, $\epsilon = 1.0e - 05$.

The first two horizontal pictures in Figure 2 present logarithmic scaled plots of the absolute value of the numerical solution v . One can see the decay $1/r^2$ at infinity guided by the black line. The next two horizontal pictures show the numerical solution scaled by a factor r^2 . Thus these graphs display vr^2 along the vertical z axis. One can observe that the scaled profile of the solution approximates a constant for large values of r . These plots are in agreement with the new boundary function \bar{v} found in (??) and with the asymptotics of the solution. Further using equation (??) for $x = 0$ or for $y = 0$ one has for sufficiently large r

$$\bar{v}(0, y) = -\frac{\mu}{y^2}, \quad \bar{v}(x, 0) = \frac{\mu}{(1 - c^2)x^2},$$

which explains the connection between the two constants displayed on the left part of Figure 2 and the right part of right Figure 2 legends. All graphs in Figure 2 show that the solution settles down as the step size h decreases, which is a visual sign of the solution's convergence.

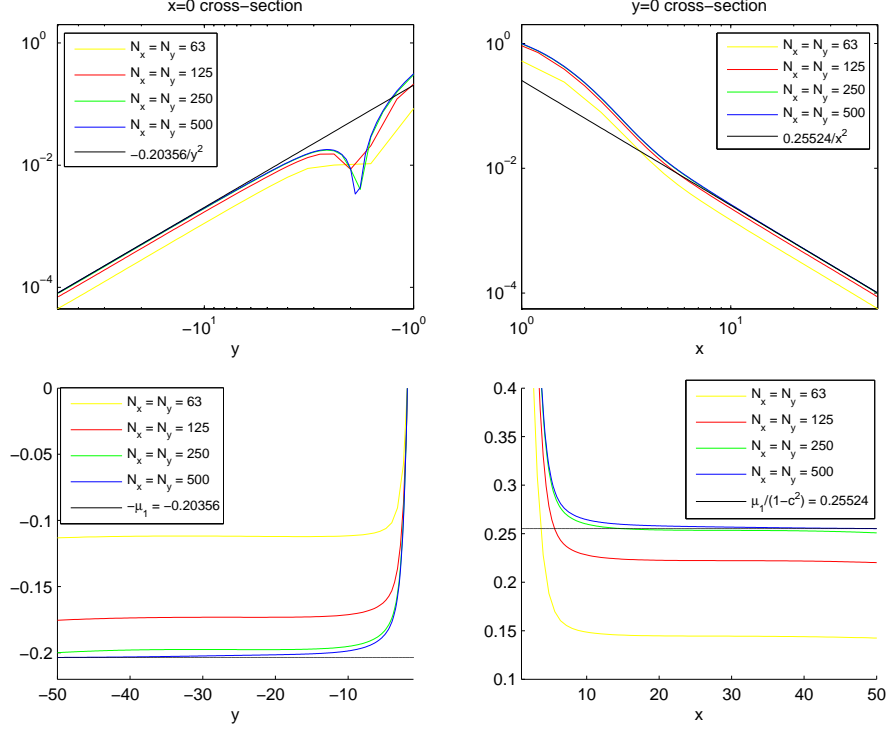


Figure 2: The effect of the mesh size. Upper panels: the function. Lower panels: the function scaled by r^2 .

5. Results

In this section we apply the presented numerical method to study the characteristic properties of the obtained numerical solution. Many parametric dependencies of the numerical solution, discovered in [7, 8], such as dependence of the solution's shape on the velocity c and on the relative dispersion parameter β , are confirmed here once again. We also compare the best-fit formulae, built up in [7], with the numerical solution developed here. Such comparison is still missing in the literature. Recall that the best-fit formulae are used as initial data for our algorithm.

5.1. Solution residual

On the left picture in Figure 3 we present the residual (??), saved on the last time level of the numerical scheme (11), for $\beta = 5$ and $c = 0.3$, while the residual, evaluated for problem with $\beta = 1$, $c = 0.9$, is demonstrated on the right part of Figure 3. Here $\epsilon = 10e - 6$ and the FDS is of 6th order of approximation. In these cases the difference between the last two iterations is $3.7749e - 007$ for the first data set and $1.2726e - 007$ for the second data set. These results show that the equation (4) is satisfied numerically with high accuracy. Note that similar

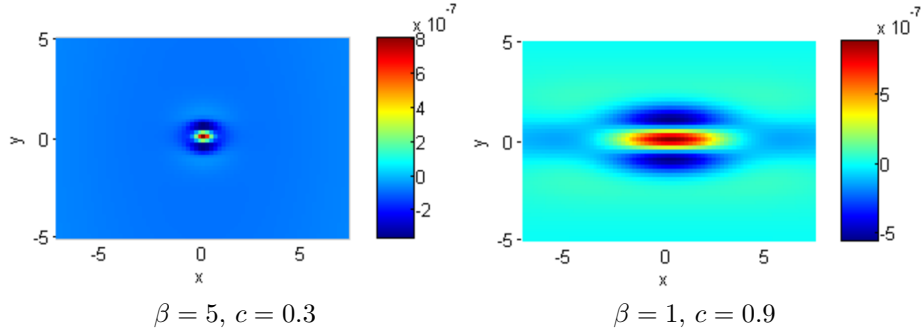


Figure 3: Residual at the last step of iteration process (11)

results about the residual for the numerical scheme in [8] are not reported there. Concerning the best-fit formulae from [7] – it is obvious to conclude from these formulae that the third, fourth and so on derivatives of the best-fit solution are unbounded in the neighborhood of the point $(0,0)$. Thus the residual, which includes fourth order derivatives of the solution, could not be considered and evaluated in the classical sense. Therefore the equation (4) is not satisfied in the neighborhood of the origin by the best-fit formulae from [7]!

FDS	h	errors in L_2	Conv. Rate	errors in L_∞	Conv. Rate
$c=0.45$ $O(h^2)$	0.8				
	0.4	2.9698e-01		4.2497e-01	
	0.2	6.8742e-02	2.1111	8.6465e-02	2.2972
$c=0.1$ $O(h^2)$	0.8				
	0.4	3.4849e-01		3.0271e-01	
	0.2	8.7696e-02	1.9905	7.5691e-02	1.9998
$c=0.45$ $O(h^6)$	0.8				
	0.4	1.0766e+00		1.2316e+00	
	0.2	3.5768e-02	4.91117	5.8927e-02	4.3855
$c=0.1$ $O(h^6)$	0.8				
	0.4	8.0095e-01		9.8911e-01	
	0.2	1.5680e-02	5.6747	2.1238e-02	5.5414

Table 3: Errors in L_2 and L_∞ norms and convergence rate for fourth order discrete derivative evaluated by FDS with $O(h^2)$ and $O(h^6)$ approximation errors

5.2. Solution derivatives

We have mentioned already that the best-fit formulae from [7] have singularities near the origin. Now we demonstrate that the discrete fourth order derivatives of the numerical solution converge numerically as the step size h

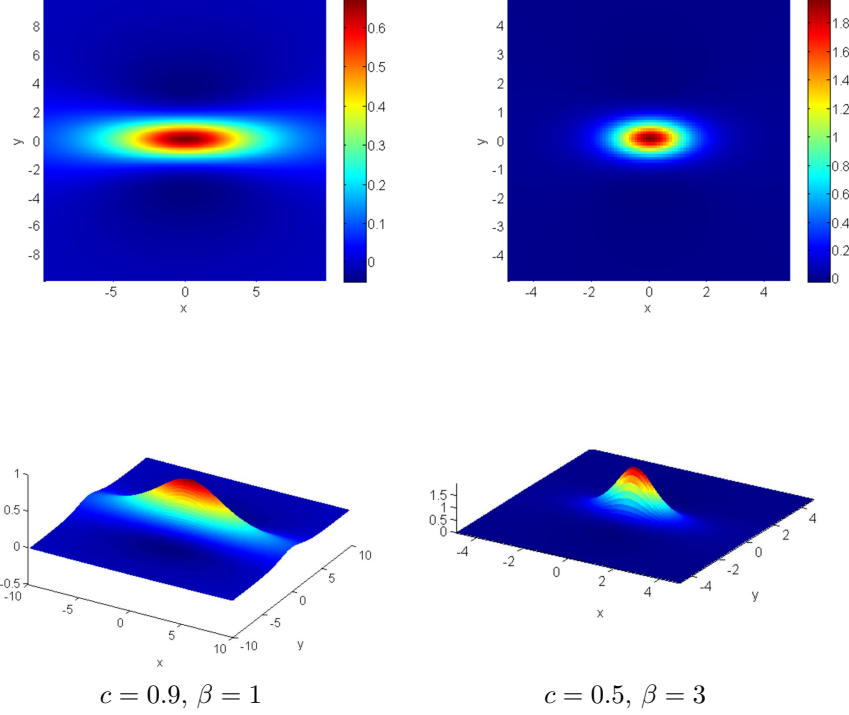


Figure 4: 2D and 3D profiles of the numerical solution

goes to zero. We apply the Runge test, evaluating the discrete fourth order derivative $\widehat{v_{xxxx}}$ of the solution on three nested meshes with step sizes h , $h/2$, $h/4$ (see Subsection (4.1)). The results are demonstrated on the next Table 3. We conclude that the discrete derivative $\widehat{v_{xxxx}}$ is bounded and converges numerically for $h \rightarrow 0$. The tests for the other fourth order derivatives are similar to the derivative v_{xxxx} and we do not present them here.

5.3. Solution shape

First, two aspects of the solution for different combinations of c and β are plotted on Figure 4. Both numerical solutions are computed on the domain $\Omega = [0, 25] \times [0, 25]$ with $h = 0.1$ and then extended symmetrically to $[-25, 25] \times [-25, 25]$. Only the essential part of the wave (near the center) is shown on these pictures. Top figures are level plots showing the waves from above and the bottom figures are three dimensional showing the structure of the wave in space. Very similar examples are presented on Figures 5 and 6, where $\Omega = [-50, 50] \times [-50, 50]$ and $h = 0.2$.

We perform a detailed study of the numerical solution's shape with respect to main parameters – the relative dispersion $\beta = \beta_1/\beta_2$ and the velocity c . Figures 5 and 6 show different aspects of the solution at $x = 0$ and $y = 0$

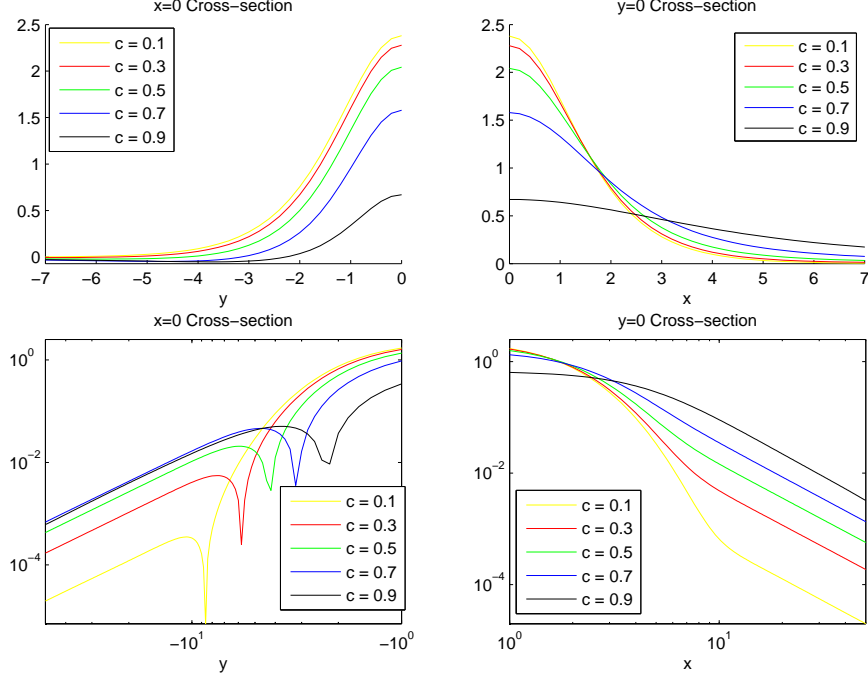


Figure 5: Cross-sections of the numerical solution for $\beta = 1$ and several c

cross-sections. The parameter α is fixed as one ($\alpha = 1$) but parameters β and c vary. We apply the computational procedure with $L_x = L_y = 50$, $h = 0.2$, $\epsilon = 1.0e - 06$. On Figure 5, parameter $\beta = 1$ is held constant and the wave dependence on the phase velocity c for $c = 0.1, 0.3, 0.5, 0.7, 0.9$ is demonstrated. Linear plots of the solution are presented on the upper row while log-log plots of the absolute value of the solution are shown on the lower part. These types of plots help us to establish the size of the computational box.

One can observe that as the phase velocity c increases the wave's support along x direction increases too, but the maximum of the wave decreases. The linear part of the solution on the log-log plots is under the governance of the boundary function. Figure 6 presents the wave dependence on the dispersion parameter $\beta = 1, 2, 3$ with fixed phase velocity $c = 0.5$. One can see that the maximum of the wave slightly decreases as β increases. The wave also becomes sharper along x and y directions. The numerical results demonstrated on Figure 5 and Figure 6 show very similar qualitative properties of the numerical solution obtained in [8] and by the numerical scheme in this paper.

5.4. Comparison with best-fit formulae from [7]

Figure 7 and Table 4 demonstrate the absolute value of the difference between the solution v^* by formulae [7] and the final solution of our procedure.

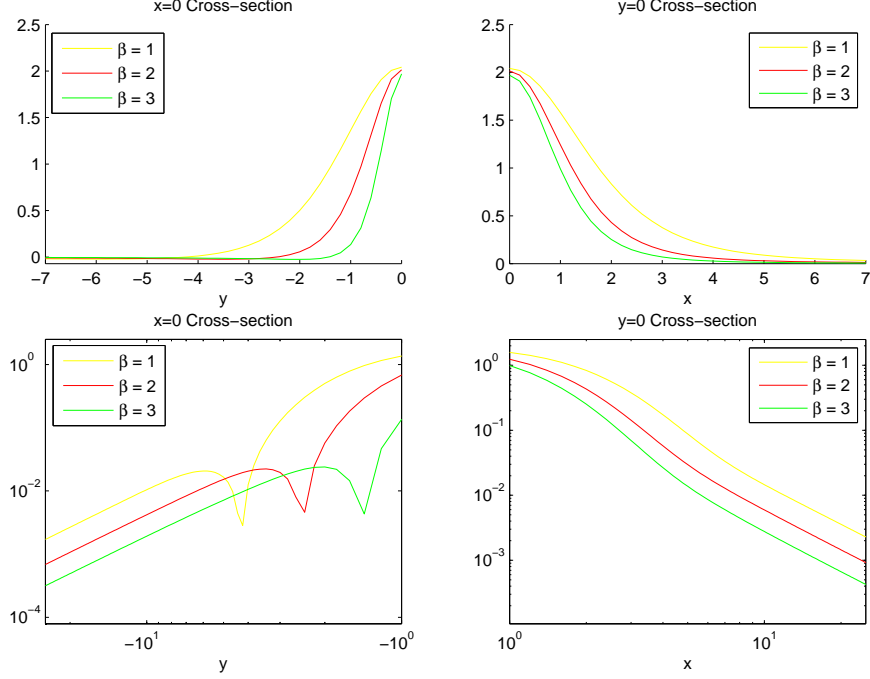


Figure 6: Cross-sections of the numerical solution for $c = 0.5$ and different β

On the left side of Figure 7 the phase velocity $c = 0.3$ is fixed and β changes. On the right side the dispersion parameter $\beta = 1$ is kept constant while c changes. The experiments are done on a $[-50, 50] \times [-50, 50]$ domain but only the results near the zero point are plotted. For each of the examples shown on Figure 7 more detailed estimate (using numbers) is given in Table 4. The difference is measured in the maximal and L_2 norms. One observes that for larger wave velocities c and dispersion parameters β the distinction becomes more pronounced. For example, for $\beta = 1$ and $c = 0.9$ the difference between the numerical solution obtained in this paper and the formulae v^* from [7] becomes ≈ 0.8 !

β	c	$\ v^* - v\ _\infty$	$\ v^* - v\ _2$
1	0.3	4.4002e-02	1.4371e-01
3		3.6519e-02	9.0714e-02
5		7.6927e-02	1.2936e-01
β	c	$\ v^* - v\ _\infty$	$\ v^* - v\ _2$
1	0.1	4.0554e-02	1.4802e-01
1	0.5	6.7063e-02	1.6766e-01
1	0.9	8.2821e-01	2.1671e0

Table 4: Differences between the numerical solution v and best-fit solution v^* from [7].

Figures 8 and 9 demonstrate the sign of the best-fit formulae v^* and the numerical solution v obtained by the presented method. The parameters of

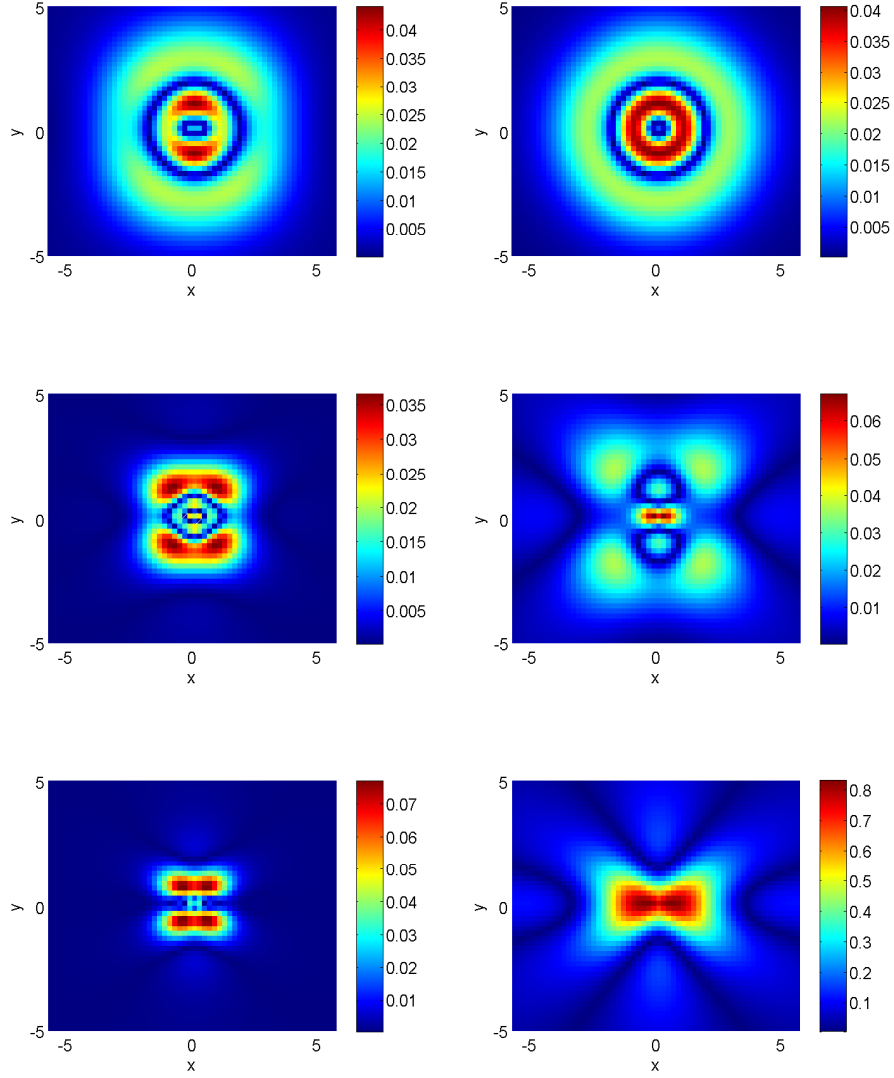


Figure 7: Difference between the numerical solution v and best fit formulae v^*

the problem are $\alpha = 1$, $\epsilon = 1.0e - 06$, $h = 0.2$ and the Laplacian is evaluated through 6th order finite differences. The colour bar is defined in the range $[-10.0e-5, 10.0e-5]$. Every value near the upper boundary and above the interval is coloured in dark red and every value near the lower boundary and below - in dark blue.

One might notice that the solution has a very peculiar shape. There exist two curves which divide the solution to 3 sub-domains: north and south domains, which are negative, and a middle, which is positive. It is obvious that far away from the zero point the solution $v(x, y) = v(r, \psi)$ obtained by this method always satisfies:

$$v(r, \psi)|_{\partial\Omega_h} \begin{cases} > 0 & \text{if } \psi \in (-\phi, \phi) \cup (\pi - \phi, \pi + \phi), \\ < 0 & \text{if } \psi \in (\phi, \pi - \phi) \cup (\pi + \phi, -\phi), \end{cases} \quad \phi = \arccos((2 - c^2)^{-0.5})$$

and the best-fit formula [7] always satisfies:

$$v(r, \psi)|_{\partial\Omega_h} \begin{cases} > 0 & \text{if } \psi \in (-\pi/4, \pi/4) \cup (3\pi/4, 5\pi/4), \\ < 0 & \text{if } \psi \in (\pi/4, 3\pi/4) \cup (5\pi/4, -\pi/4). \end{cases}$$

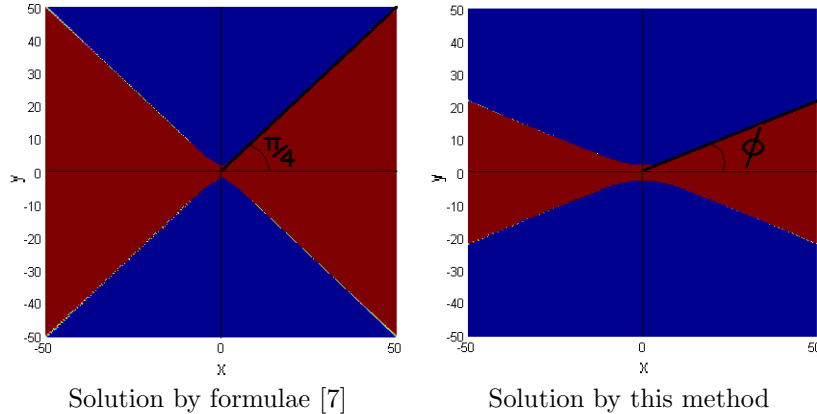


Figure 8: Sign of the solutions, $c = 0.9$, $\beta = 1$

Notice that for smaller velocities $c \in [0, 0.57]$ the relation $\phi \in [\pi/4 - \pi/30, \pi/4 + \pi/30]$ holds for ϕ . Recall the restriction $c \in \min(1, 1/\sqrt{\beta})$ made in the beginning of the paper. Thus larger β 's have impact on the velocity interval which reflects on the angle ϕ and thus on the positive/negative domain coverage. E.g. on Figure 9 with $\beta = 3$, for the solution we have that $\phi \approx \pi/4$. But for $\beta = 1$ and $c = 0.9$ (see Figure 8) there is a big difference between positive/negative parts of the solution obtained here and in [7]! It is obvious that our solution v and the best-fit formulae v^* from [7] differ when compared to this characteristic - for some cases significantly, for others - slightly.

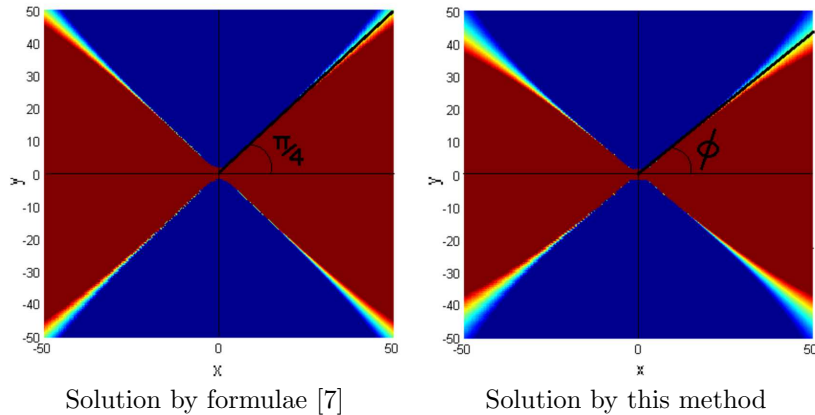


Figure 9: Sign of the solutions, $c = 0.5$, $\beta = 3$

6. Conclusion

Fourth and sixth order finite difference schemes are applied for numerical evaluation of the travelling wave solutions to the Boussinesq equation in this paper. New conditions on the computational boundaries are devised. The high accuracy of the method applied is demonstrated on several experiments. The numerical solution obtained here performs similarly to the numerical solutions given in [7, 8] with respect to solution shape and the dependence on the velocity c and relative dispersion β . The best-fit approximation formulae from [7] fail to satisfy the initial equation in the classical sense in the neighborhood of the origin. In the future, we will exploit the obtained numerical traveling wave solutions as initial data to the corresponding Boussinesq equation in order to seek two dimensional solitary wave solutions to (1).

References

- [1] J. Choudhury, C. Christov, 2D Solitary waves of Boussinesq equation, CP75, (2005) 8590.
- [2] A. Chertock, C. Christov, A. Kurganov, Central-upwind schemes for the Boussinesq paradigm equation, Comp. Sci. High Performance Comp. IV, NNFM, 113, (2011) 267281.
- [3] M. Christou, C. I. Christov, FourierGalerkin method for 2D solitons of Boussinesq equation, Mathematics and Computers in Simulation 74 (2007) 8292.
- [4] M. Christou, C. I. Christov, Galerkin Spectral Method for the 2D Solitary Waves of Boussinesq Paradigm Equation, CP 1186 (2009) 217 – 225.

- [5] C. I. Cristov, Conservative difference scheme for Boussinesq model of surface waves, Proc. ICFDS Oxford (1996) 343–349.
- [6] C. I. Christov, An energy-consistent dispersive shallow-water model, Wave Motion, 34, (2001) 161 – 174
- [7] C. I. Christov, J. Choudhury, Perturbation solution for the 2D Boussinesq equation, Mech. Res. Commun., 38 (2011) 274 – 281.
- [8] C. I. Christov, Numerical implementation of the asymptotic boundary conditions for steadily propagating 2D solitons of Boussinesq type equation, Math. Computers Simul., 82 (2012) 1079 – 1092.
- [9] C. Christov, N. Kolkovska, D. Vasileva, On the numerical simulation of unsteady solutions for the 2D Boussinesq paradigm equation, LNCS, 6046 (2011) 386 – 394.
- [10] B. Fornberg, Generation of Finite Difference Formulas on Arbitrarily Spaced Grids, Math. Comput., 51(1988), 699 – 706.
- [11] A. Samarskii, The theory of difference schemes, M. Dekker, 2001.